ADVANCED MATERIALS
www.advmat.de

Monolithic Zirconium-Based Metal–Organic Frameworks for Energy-Efficient Water Adsorption Applications

*Ceren Çamur, Robin Babu, José A. Suárez del Pino, Nakul Rampal, Javier Pérez-Carvajal, Philipp Hügenell, Sebastian-Johannes Ernst, Joaquin Silvestre-Albero, Inhar Imaz, David G. Madden, Daniel Maspoch, and David Fairen-Jimenez**

Space cooling and heating, ventilation, and air conditioning (HVAC) accounts for roughly 10% of global electricity use and are responsible for ca. 1.13 gigatonnes of CO_2 emissions annually. Adsorbent-based HVAC technologies have long been touted as an energy-efficient alternative to traditional refrigeration systems. However, thus far, no suitable adsorbents have been developed which overcome the drawbacks associated with traditional sorbent materials such as silica gels and zeolites. Metal–organic frameworks (MOFs) offer order-of-magnitude improvements in water adsorption and regeneration energy requirements. However, the deployment of MOFs in HVAC applications has been hampered by issues related to MOF powder processing. Herein, three high-density, shaped, monolithic MOFs (UiO-66, UiO-66-NH_2, and Zr-fumarate) with exceptional volumetric gas/vapor uptake are developed—solving previous issues in MOF-HVAC deployment. The monolithic structures across the mesoporous range are visualized using small-angle X-ray scattering and lattice-gas models, giving accurate predictions of adsorption characteristics of the monolithic materials. It is also demonstrated that a fragile MOF such as Zr-fumarate can be synthesized in monolithic form with a bulk density of 0.76 gcm^{-3} without losing any adsorption performance, having a coefficient of performance (COP) of 0.71 with a low regeneration temperature (≤ 100 °C).

1. Introduction

We are currently living in one of the warmest periods in recorded climate history. With these increases in global temperatures, the demand for heating, ventilation, and air conditioning (HVAC) has steadily increased over the past three decades. Worldwide, there are currently about 1.6 billion air conditioning (AC) units in use, consuming over 2000 terawatt-hours (TWh) or roughly 10% of the 21 000 TWh of electricity consumed globally in 2016.[1] The increase in demand for cooling can be attributed to a wide variety of applications, including domestic and office AC units, server farm cooling, and industrial heat exchangers. In 2017, there were approximately 8 million data centers around the world that consumed 416.2 TWh of electricity.[2] This equated to 2% of global electricity consumption of which 38% of this consumption was consumed by AC systems.[3] The high energy consumption of existing HVAC technologies comes with a significant penalty in terms of their environmental footprint.

C. Çamur, R. Babu, N. Rampal, D. G. Madden, D. Fairen-Jimenez
The Adsorption & Advanced Materials Laboratory (A2ML)
Department of Chemical Engineering & Biotechnology
University of Cambridge
Philippa Fawcett Drive, Cambridge CB3 0AS, UK
E-mail: df334@cam.ac.uk

The ORCID identification number(s) for the author(s) of this article can be found under https://doi.org/10.1002/adma.202209104

[+]Present address: Instituto de Ciencia de Materiales de Madrid, Consejo Superior de Investigaciones Científicas (ICMM-CSIC), 28049 Madrid, Spain

DOI: 10.1002/adma.202209104

J. A. Suárez del Pino, J. Pérez-Carvajal[+], I. Imaz, D. Maspoch
Catalan Institute of Nanoscience and Nanotechnology (ICN2)
CSIC and the Barcelona Institute of Science and Technology Campus UAB
Bellaterra, Barcelona 08193, Spain

J. Pérez-Carvajal[+]
Laboratoire de Physique de l'Ecole Normale Supérieure-ENS
Université PSL
CNRS
Paris 75005, France

P. Hügenell, S.-J. Ernst
Fraunhofer-Institute for Solar Energy Systems (ISE)
Heidenhofstr. 2, 79110 Freiburg, Germany

J. Silvestre-Albero
Laboratorio de Materiales Avanzados
Depto. de Química Inorgánica
Universidad de Alicante
San Vicente del Raspeig E-03690, Spain

D. Maspoch
ICREA
Pg. Lluís Companys 23, Barcelona 08010, Spain

The demand for AC units is expected to triple to 5.6 billion by 2050 as global populations rise and the demand for HVAC increases.[4] The rising demand for HVAC in the coming decades will require a significant shift in terms of energy efficiency to enable sustainable cooling in the future.

Traditional HVAC technologies employ energy-intensive dehumidification processes that require incoming air to be cooled to the dew point of moisture (ca. 5–7 °C) to enable condensation. As an alternative to the traditional chiller technology, adsorption-driven heat transformation (AHT) systems have long been touted for energy-efficient cooling systems, raising the evaporation temperature to ambient temperatures (ca. 20–25 °C), which in turn can improve the coefficient of performance (COP) of the entire system.[5] The AHT process of heating and cooling is based on an adsorption–desorption cycle of a working fluid that consists of four steps: isosteric heating (B→C), isobaric desorption (C→D), isosteric cooling (D→A), and isobaric adsorption (A→B) (**Figure 1**). In the adsorption cycle (Figure 1, Step 1 and Step 2), the effective cold is produced during the evaporation of the working fluid (Q_{ev}) as the process is endothermic. Concurrently, the useful heat (Q_{ads}) is released by the adsorption of the produced vapor. As the adsorbent will be saturated after a while, the desorption of the working liquid—in other words, the regeneration of the adsorbent—will be required. In the desorption cycle (Figure 1, Step 3 and Step 4), the energy (Q_{des}) is used to desorb the working fluid at a temperature (T_{des}). The desorbed working fluid condenses by producing useful heat (Q_{con}).[6–8] For chilling applications here, the facile regeneration of adsorbent materials at low temperature ($T_{des} \leq 100$ °C) and a step between 10% and 30% RH are a critical requirement to develop AHT systems with optimum efficiency.[9,10]

Commercially available AHT pumps currently employ traditional porous adsorbents such as silicas and zeolites. While these materials work on this application, their limitations in terms of tunability limit their performance and potential for further development. Additionally, many traditional adsorbents require high temperatures for regeneration (e.g., T_{des}>180 °C for zeolites), which in turn can dramatically reduce the COP—silica gel = 0.35 and zeolite 4A = 0.56—of the AHT system.[11,12] The lack of suitable adsorbents is currently the major limiting factor in the development of solid adsorbent dehumidification systems.

As an alternative to traditional adsorbents, MOFs[13,14] have garnered significant attention recently for water adsorption applications. There are currently more than 100 000 MOF[15,16] structures in existence versus ca. 1000 silica's and zeolites; their tunable nature enables precise control of material design at the molecular level. This, in addition to their extremely high pore volumes, can enable the design of materials with ultra-high porosity and optimal MOF–water interactions, making them ideally suited for overcoming issues related to water adsorption capacities and regeneration energies. The use of MOFs for water capture and dehumidification applications has only recently been investigated, partly due to the development of MOFs with superior thermochemical and hydrolytic stability.[17] To date, MOFs have displayed benchmark performance for a wide variety of water adsorption applications, including atmospheric water harvesting, adsorbents-based chillers, and adsorbent-based heat pumps due to their characteristic Type V, S-shaped isotherms (Figure S1, Supporting Information).[18–26] Studies on MOF-based adsorbent refrigeration have seen significant improvements in COP (e.g., MIP-200 = 0.81)[23] when compared with zeolites[27] and silicates.[11] Similarly, the use of MOFs has seen dramatic reductions in the heat requirements for adsorbent regeneration (≤100 °C) compared to zeolites.[28]

The integration of adsorption materials in AHT devices is only possible after some specific shaping processes to obtain optimum performance.[27,29] Since MOFs are traditionally produced as powders, their shaping is crucial for integration into industrial processes.[26] Numerous shaping techniques have been reported to produce MOFs as granules, pellets, and foams.[30,31] However, the loss of surface area and porosity during densification and shaping (between 14% and 64%) compared to powders remains a major issue in MOF deployment in the industry.[32,33] These reductions in performance can be associated with the incorporation of dead volume through the use of binders and/or the structural collapse of the MOF structure and porosity as a result of the high mechanical pressure.[26,34–36] Even more important, pelletized MOFs using lower mechanical pressures to avoid pore collapse suffer from low bulk densities due to particle packing inefficiencies. In contrast, the recent development of so-called monolithic MOFs ($_{mono}$MOFs)[37] has led to a paradigm shift in terms of MOF shaping. We have reported the sol–gel synthesis of several $_{mono}$MOFs ($_{mono}$UiO-66, $_{mono}$HKUST-1, and $_{mono}$ZIF-8)[32,37,38] as shaped bodies up to about 1 cm^3 in size without using supports, applied mechanical pressures, or binders. The synthesis of $_{mono}$MOFs represents a viable route towards industrial production of MOFs in high-density, shaped bodies while preserving the full adsorption performance of the material. The development of $_{mono}$MOFs has already given way to materials that demonstrate benchmark performance in terms of natural gas and hydrogen storage.[32,37,39]

In this contribution, we investigate the water adsorption performance of $_{mono}$MOFs for HVAC applications. We have previously demonstrated that Zr-based MOF UiO-66 (UiO = Universitetet i Oslo), is amenable to high-density $_{mono}$MOF formation. Herein, we extend our sol–gel approach to synthesize and assess the water adsorption performance of three monolithic Zr-MOFs, $_{mono}$UiO-66, $_{mono}$UiO-66-NH_2, and $_{mono}$Zr-fumarate, comparing them to their powder and pelletized forms. Among these three materials, we have already published $_{mono}$UiO-66 and $_{mono}$UiO-66-NH_2 for gas storage applications whereas $_{mono}$Zr-fumarate has been synthesized for this study. These materials feature large hydrophilic channels in their crystal structure, which leads to outstanding water-adsorption properties. This includes a high uptake of water in a low relative pressure range, characteristic Type V (i.e., S-shaped) isotherms facile desorption at fairly low temperatures, and high COP for chillers.[25,40] Then, we evaluate the performance of the six adsorbents (powders and monoliths) from single-component water adsorption isotherms, adsorption enthalpy (ΔH_{ads}), and COP calculations, kinetics studies, and adsorption–desorption cyclability testing. Finally, using a lattice-gas model based on the combination of small-angle X-ray scattering (SAXS) and grand canonical Monte Carlo molecular simulations, we reveal the monolithic structure of the materials across the mesoporous range.

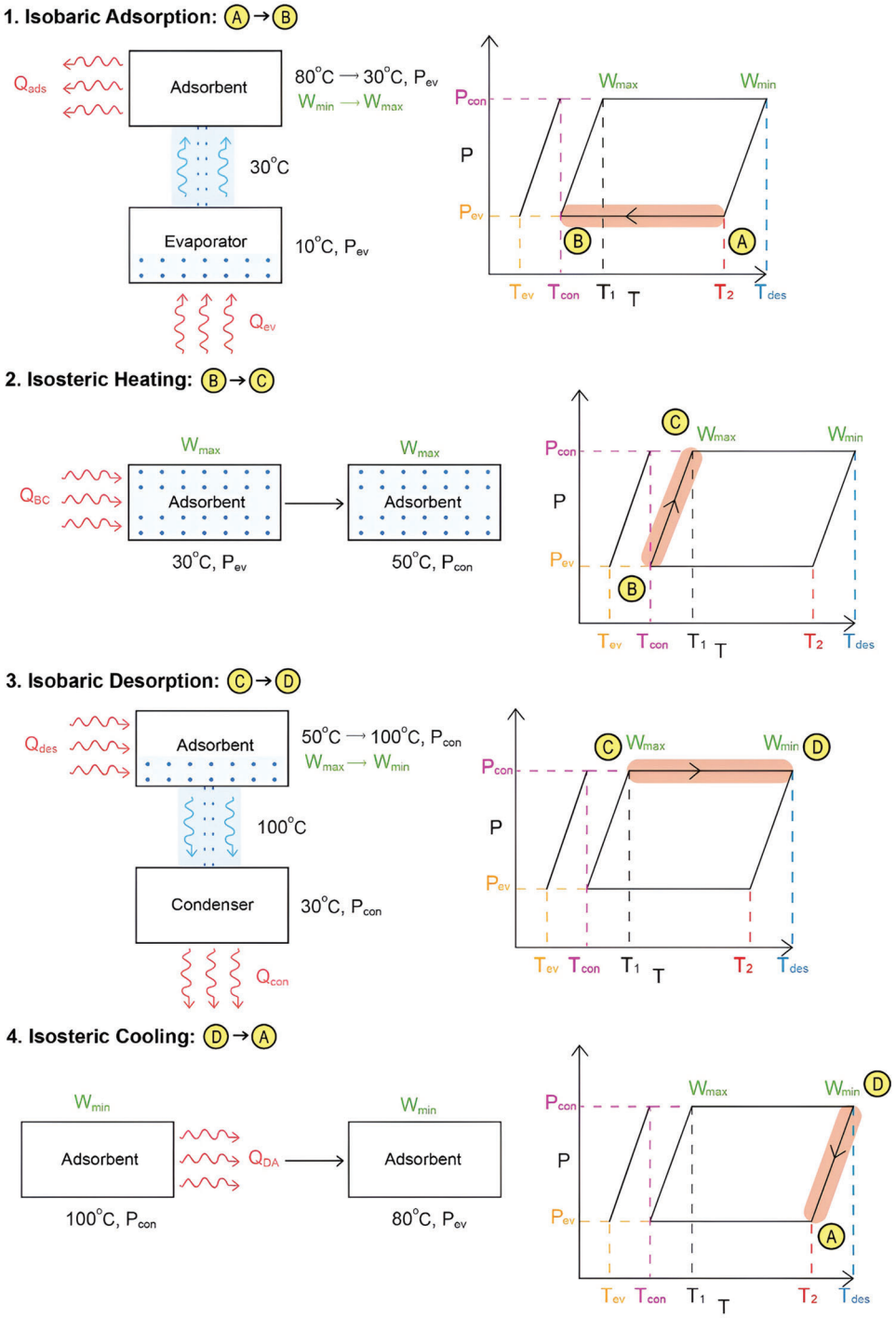

Figure 1. Operation principle of an AHT pump. Isosteric diagram of an AHT pump cycle of the adsorption (Step 1 and Step 2) and the desorption (Step 3 and Step 4) cycles where the operating temperature and pressure of the evaporator are fixed at T_{ev} = 10 °C and P_{ev} = 1.23 kPa, and the operational temperature and pressure of the condenser are fixed at T_{con} = 30 °C and P_{con} = 4.25 kPa. In Step 1 (isobaric adsorption, A→B), the working fluid (water) is heated from 10 °C (T_{ev}) to 30 °C (T_{con}), using energy equivalent to Q_{ev} coming from the surroundings (effective cooling). Here, the adsorbent loading increases from W_{min} to W_{max}, while the temperature of the adsorbent reduces from 80 (T_2) to 30 °C (T_{con}), giving out energy equivalent to Q_{ads}. In Step 2 (isosteric heating, B→C), the adsorbent is heated from 30 (T_{con}) to 50 °C (T_1), using energy equivalent to Q_{BC}, while at the same time, pressure increases from P_{ev} to P_{con}; adsorbent loading remains unchanged at W_{max}. In Step 3 (isobaric desorption, C→D), the adsorbent is heated from 50 (T_1) to 100 °C (T_{des}), using energy equivalent to Q_{des} or, in other words, Q_{reg}, while at the same time, the adsorbent loading reduces from W_{max} to W_{min}, and an energy equivalent to Q_{con} is given out to the surroundings (effective heating). In Step 4 (isosteric cooling, D→A), the adsorbent is cooled from 100 (T_{des}) to 80 °C (T_2), giving out energy equivalent to Q_{DA}, while at the same time, the pressure reduces from P_{con} to P_{ev}; adsorbent loading remains unchanged at W_{min}.

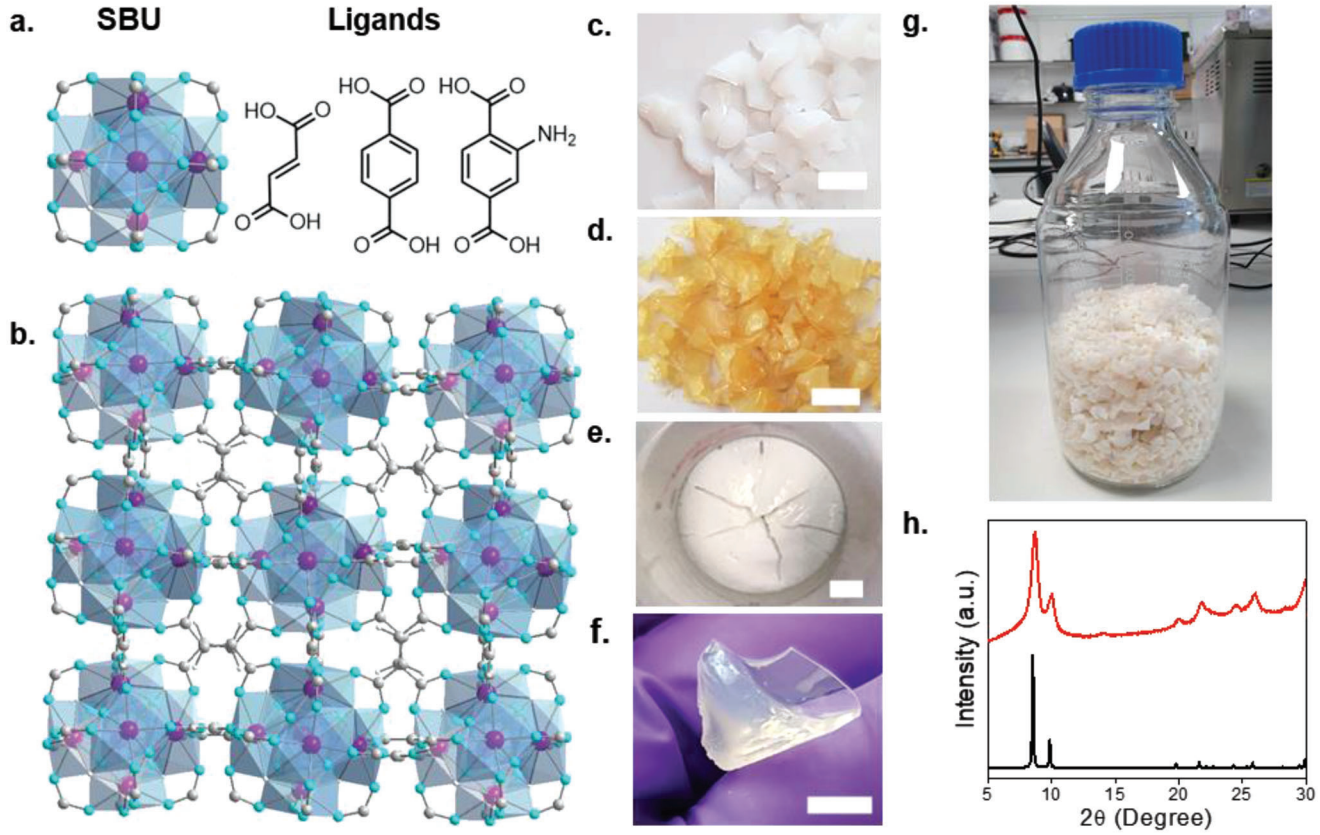

Figure 2. Zr-based MOFs UiO-66, UiO-66-NH_2, and Zr-fumarate. a) The secondary building unit (SBU) of the UiO-family and ligands (fumaric acid, terephthalic acid, and 2-aminoterephthalic acid, respectively, from left to right) employed. b) Zr-fumarate structure (purple, zirconium; cyan, oxygen; gray, carbon; and white, hydrogen). c–f) Optical images of $_{mono}$UiO-66 (c), $_{mono}$UiO-66-NH_2 (d), Zr-fumarate gel (e), and $_{mono}$Zr-fumarate (f) (scale bars = 0.5 cm). g) Optical image of the gram-scale (335 g) $_{mono}$Zr-fumarate product in a 500 mL bottle. h) Experimental PXRD pattern of $_{mono}$Zr-fumarate (red) compared to the simulated one (black).

2. Synthesis, Characterization, and Scale-Up

Zr-based MOFs such as the UiO-family are promising materials for HVAC applications due to their high thermal and chemical stability, and large porosity. UiO-type MOFs consist of Zr-oxo clusters linked together by carboxylate-based ligands (L), such as terephthalic acid (BDC), 2-aminoterephthalic acid (ABDC) and fumaric acid (FA), to give the overall composition of $[Zr_6O_4(OH)_4(L)_6]_n$ (**Figure 2**a,b). Herein, we have studied three different sets of samples: monolithic (mono), standard powders (powd), and pelletized (pell) samples. $_{mono}$UiO-66 and $_{mono}$UiO-66-NH_2 were synthesized via previously reported methods.[37] In a typical synthesis, MOF primary nanoparticles are successfully densified using mild drying conditions to yield centimeter-scale monoliths (Figure 2c,d). The new monolithic material, $_{mono}$Zr-fumarate, was produced by using the same procedure previously described for powder form[41] (Figure 2e). After the colloidal solution was formed, we washed the material several times through centrifugation by using acetone and ethanol. Then, the collected Zr-fumarate gel was dried at ambient conditions slowly overnight or longer depending on the amount of the gel to form $_{mono}$Zr-fumarate (Figure 2f). Before scaling up this procedure, we checked the reproducibility of the different batches by comparing the porosity of the produced $_{mono}$Zr-fumarate. The N_2 adsorption isotherms at 77 K show similar microporosity and small changes in the mesoporosity for three different batches (Figure S2, Supporting Information). Then, this procedure was found to be scalable, whereby a 1 L batch reaction was found to produce ca. 67 g (≈75% yield) of $_{mono}$Zr-fumarate. To confirm the scalability of the process, we reproduced the 1 L batch reaction five times, which resulted in 335 g (Figure 2g). Powder forms of UiO-66, UiO-66-NH_2, and Zr-fumarate ($_{powd}$UiO-66, $_{powd}$UiO-66-NH_2, and $_{powd}$Zr-fumarate) were synthesized using similar procedures but including fast overnight drying at 100 °C under vacuum. To achieve an extensive comparison, we used the already published physical properties for the pelletized form of UiO-66, UiO-66-NH_2, and Zr-fumarate ($_{pell}$UiO-66, $_{pell}$UiO-66-NH_2, and $_{pell}$Zr-fumarate).[34,35] We utilized powder X-ray diffraction (PXRD) to confirm the structures of all synthesized materials. Figure 2h and Figure S3, Supporting Information, show the PXRD patterns for the $_{mono}$MOFs produced, displaying a clear Scherrer line broadening, caused by the non-convergence of the diffraction line in nano-sized particles. Field electron scanning electron microscopy (FE-SEM) further confirmed that the produced $_{mono}$Zr-MOFs comprise densified MOF nanoparticles with particle sizes of 20 ± 4.5, 19 ± 3.6, and 25 ± 5 nm for $_{mono}$UiO-66, $_{mono}$UiO-66-NH_2, and $_{mono}$Zr-fumarate, respectively (Figure S4, Supporting Information). Figure S5, Supporting Information, shows the

Table 1. Experimental and simulated textural, physicochemical, and water adsorption properties of monolithic (mono), and powdered (powd) samples, as well as molecular simulation (sim) for the Zr-MOFs, studied. Pelletized (pell) data is taken from the literature.

Materials	S_{BET}[a] [$m^2\ g^{-1}$]	S_{BET}(v)[b] [$m^2\ cm^{-3}$]	W_0[c] [$cm^3\ g^{-1}$]	V_{tot}[d] [$cm^3\ g^{-1}$]	ρ_b[e] [$g\ cm^{-3}$]	H_2O uptake at 25 °C					
						RH [%] = 10		RH [%] = 30		RH [%] = 90	
						[$g\ g^{-1}$]	[$g\ cm^{-3}$]	[$g\ g^{-1}$]	[$g\ cm^{-3}$]	[$g\ g^{-1}$]	[$g\ cm^{-3}$]
$_{mono}$UiO-66	1223	905	0.47	1.59	0.74	0.07	0.05	0.20	0.15	0.41	0.30
$_{powd}$UiO-66	1223	635	0.50	2.05	0.52	0.07	0.03	0.20	0.10	0.42	0.21
$_{pell}$UiO-66[35]	1459	627	0.54	–	0.43	–	–	–	–	–	–
$_{sim}$UiO-66	1120	1413	0.39	–	1.62	–	–	–	–	–	–
$_{mono}$UiO-66-NH_2	988	1027	0.38	1.47	1.04	0.10	0.10	0.18	0.19	0.48	0.50
$_{powd}$UiO-66-NH_2	1094	645	0.42	0.94	0.59	0.11	0.07	0.20	0.13	0.27	0.17
$_{pell}$UiO-66-NH_2[35]	816	408	0.33	–	0.50	–	–	–	–	–	–
$_{sim}$UiO-66-NH_2	897	1063	0.39	–	1.28	–	–	–	–	–	–
$_{mono}$Zr-fumarate	854	649	0.33	0.90	0.76	0.15	0.12	0.26	0.21	0.39	0.31
$_{powd}$Zr-fumarate	868	469	0.33	1.39	0.54	0.09	0.09	0.21	0.14	0.44	0.26
$_{pell}$Zr-fumarate[26,34]	569–479	–	–	–	–	–	–	–	–	–	–
$_{sim}$Zr-fumarate	821	1429	0.28	–	1.74	–	–	–	–	–	–

[a] BET area (S_{BET}); [b] Volumetric BET area (S_{BET}(v)); [c] Micropore volume (W_0) obtained at $P/P_0 = 0.1$; [d] Total pore volume (V_{tot}) obtained at $P/P_0 = 0.98$; [e] Bulk density (ρ_b) quantified using Hg-porosimetry.

thermogravimetric analysis (TGA) of the $_{mono}$MOF samples, with monolith decomposition occurring at temperatures higher than 250 °C.

Figure S6, Supporting Information, shows the experimental N_2 adsorption isotherms at 77 K for monolithic and powder samples as well as obtained from grand canonical Monte Carlo (GCMC) simulations. **Table 1** shows the BET areas (S_{BET}) of pelletized samples taken from the literature[26,34,35] and synthesized samples calculated using the extended Rouquerol's criteria implemented in BETSI,[42] (Figures S7–S13, Supporting Information) as well as the micropore (W_0) and total (V_{tot}) pore volumes, bulk (mercury) density, and water uptakes at different relative humidities.[43] There are no significant differences between powder and monolithic materials in the micropore region and in terms of the calculated S_{BET} values. However, compared to the GCMC isotherms, the experimental samples have higher S_{BET} and W_0 than the theoretical maximum for defect-free $_{sim}$UiO-66, $_{sim}$UiO-66-NH_2, and $_{sim}$Zr-fumarate. This is the result of the presence of modulators in the synthesis and missing linkers in the final structures. Indeed, calculated defect-free S_{BET} using GCMC simulations are also close to the original report of UiO-66 (Lillerud and co-workers, 1187 $m^2\ g^{-1}$),[44] and reports on UiO-66-NH_2 (Farha and co-workers, 800 $m^2\ g^{-1}$)[45] and Zr-fumarate (Yaghi et al. and co-workers, 690 $m^2\ g^{-1}$).[40] For all the materials, we obtained high gas uptakes below 0.1 P/P_0, indicating the presence of extensive microporosity. We also found N_2 uptake increases at higher relative pressures, indicating the existence of mesoporosity. The NLDFT pore-size distributions (PSD) highlight the substantial micropore volume, whereas the BJH analysis confirms significant volumes of wide mesoporosity, varying between 10 and 30 nm for the monoliths and 10 and 15 nm for powders encountered due to the inherent assembly of the nanoparticles (Figure S14, Supporting Information).

The use of modulators is related to an increase in the number of framework defects in Zr-MOFs, forming narrow mesopores due to missing linkers or metal clusters.[45] To examine the missing linkers in the structures of $_{mono}$Zr-MOFs, we used X-ray photoelectron spectroscopy (XPS) to quantify Zr/C ratio for each material, CHN combustion through inductively coupled plasma-optical emission spectrometry (ICP-OES) to quantify atomic Zr%, C%, and N%, and nuclear magnetic resonance (^{1}H-NMR). Figures S15–S17, Supporting Information, show the XPS results; Table S4, Supporting Information, show the main results. Together, we observed an increase in the Zr/C ratio for $_{mono}$UiO-66, $_{mono}$UiO-66-NH_2, and $_{mono}$Zr-fumarate, which are 0.11, 0.11, and 0.13, respectively, compared to Zr/C ratios of defect-free structures, that is, 0.06, 0.06 and 0.12, respectively. Literature attributed these changes to missing linker defects due to the C decrease in the structure.[44,46] Table S5, Supporting Information, shows the CHN combustion analysis from ICP-OES, which verifies these findings. From the ^{1}H-NMR studies, we also found that the molar ratios of acetate/ligand in the structures were 0.13, 0.16, and 0.13 for $_{mono}$UiO-66, $_{mono}$UiO-66-NH_2, and $_{mono}$Zr-fumarate, respectively. These results are similar to those previously reported for powder samples (Figure S18, Supporting Information).[47,48]

We then analyzed the packing efficiency of the monolithic and powder materials, measuring their bulk densities (ρ_b) through mercury intrusion porosimetry, a technique based on Archimedes' principle that can also probe the macro and mesoporosity of the samples; Table 1 shows the densities and Figure S19, Supporting Information, shows the mercury intrusion pore size distributions. From the comparison of $_{mono}$MOFs and powders, the critical advantage of monolithic materials is their high bulk density, which translates to higher volumetric S_{BET}, pore volumes, and adsorption capacities compared to their

traditional powder counterparts. Even though the synthesized powder samples have similar gravimetric S_{BET} values to monolithic materials, $_{mono}$UiO-66, $_{mono}$UiO-66-NH_2, and $_{mono}$Zr-fumarate show 28%, 49%, and 30% higher volumetric N_2 gas adsorption capacity and, therefore, volumetric S_{BET}, than their powder counterparts (Figure S6d–f, Supporting Information). As we have explained elsewhere, the high density of the monoliths arises from the efficient packing of MOF primary particles within the monolithic macrostructure.[32,33] On the other hand, the interparticle space present within the body of powders but also of pellets reduces the bulk density of the materials. Densification and pelletization of UiO-66, UiO-66-NH_2, and Zr-fumarate powders have been previously reported under a variety of pressures with and without binders.[34,35] In our case here, as a result of the pelletization, these materials show higher bulk densities. However, the use of pressure usually brings together a reduction in the gravimetric BET area.[34,35] In comparison to the pelletized samples, $_{mono}$UiO-66, $_{mono}$UiO-66-NH_2, and $_{mono}$Zr-fumarate exhibit exceptional bulk densities (Table 1).

3. Small-Angle X-ray Scattering and Lattice-Gas Models

To fully understand the porous texture and structure of our monoliths as well as the contributions to the total gas uptake arising from inter-particle mesopores, we used small-angle X-ray scattering (SAXS) and lattice-gas models. **Figure 3**a–f shows the experimental SAXS curves, the fits based on a spherical form factor model, and the particle size distributions; Table S3, Supporting Information, summarizes the results. Since the Guinier regions of these materials—the region which describes the radius of gyration (R_g) of the particles—lie outside the range probed, we used instead a simplified power law based on Porod's law given by Equation (1):

$$I\ (Q) = B(Q)^{-P} \tag{1}$$

where B is the prefactor and P is the power-law exponent, fitted to the slope of I(Q) in the low-Q region. The power-law exponents for $_{mono}$UiO-66 and $_{mono}$Zr-fumarate are 3.035 and 3.111, respectively, indicating the presence of surface fractals, whereas for $_{mono}$UiO-66-NH_2 the power-law exponent is 2.895, indicating the presence of mass fractals. Importantly, the particle size distributions for $_{mono}$UiO-66 and $_{mono}$UiO-66-NH_2 are similar, exhibiting two main particle size populations of mean diameters ≈80 and ≈160 Å. In addition, a small volume fraction of the particles in $_{mono}$UiO-66-NH_2 exhibits a mean diameter of 234 Å. For $_{mono}$Zr-fumarate, we see one main population of particles with a mean diameter of 76 Å, and an equivalent volume fraction of particles having mean diameters of 167, 252, 339, and 424 Å.

Anticipating the performance of the different samples on water adsorption, as described below, we decided to focus on the top-two performing materials for the lattice-gas models, and hence excluded UiO-66-NH_2. Lattice-gas models have been widely used to investigate the nature of adsorption hysteresis for fluids trapped in interconnected void spaces of porous glasses.[46,47] Using the SAXS data for $_{mono}$UiO-66 and $_{mono}$Zr-fumarate, a two-point correlation function $S_2(r)$ was generated, which was then used to create a 3D reconstruction of the monoliths. Figure 3g and Figure 3h show the $S_2(r)$ of the target and reconstructed medium for both materials; Figure 3j,k shows the 3D reconstruction of the lattice-gas models for the activated $_{mono}$UiO-66 and $_{mono}$Zr-fumarate, respectively—for each structure, the gray voxels are the cells occupied by the material and white voxels correspond to the porosity of the material. Figure 3i,l shows the comparison of experimental and GCMC simulated N_2 isotherms obtained on different models for UiO-66 and Zr-fumarate, respectively. GCMC simulations on a perfect structure can only capture, as expected, the microporosity of both MOFs—this approach works well for structures with perfect packing. But, in the case of the monoliths, we see an additional slope in the isotherm associated with the porosity that arises due to the random packing of the particles—this extrinsic porosity is not accessible using GCMC simulations alone. To describe the isotherm for the monolith across the entire p/p_0 range sampled, GCMC computed isotherms must be complemented with isotherms calculated using the lattice-gas models. Hence, to model the trajectory of the system in the grand canonical ensemble, we employed kinetic Monte Carlo simulations to obtain the nitrogen adsorption isotherms. From the $_{mono}$Zr-fumarate and $_{mono}$UiO-66 isotherms generated, we found an excellent agreement between experiment and theory within the high-pressure region ($p/p_0 > 0.6$) of the adsorption isotherm, providing complementary data to the pure GCMC-calculated isotherms. This demonstrates the applicability of lattice-gas models in capturing the accessible extrinsic, inter-particle mesoporosity of $_{mono}$MOFs. Collectively, these results suggest that the hierarchical porosity of $_{mono}$Zr-MOFs can be accurately described computationally across the micro- and mesoporous range, enabling robust future predictions of adsorption characteristics.

4. HVAC Applications

With the materials characterized, we moved to the determination of the water adsorption properties of the powdered and $_{mono}$MOF materials. We initially performed single-component water adsorption isotherms. The powdered MOFs illustrated characteristic water adsorption isotherms similar to those previously reported in the literature for each material. Importantly, $_{mono}$MOFs retained high water uptake associated with the powdered variants of each material (**Figure 4**a).[40] The narrow and hydrophilic pores in $_{mono}$Zr-fumarate give way to a steep increase in the water uptake in the 5%–30% relative humidity (%RH) range of the Type V isotherm. Increasing the length of the linker through isoreticular chemistry increases the hydrophobicity of the $_{mono}$MOF, leading to a shift of the inflection point (α) from ca. 8% RH to ca. 25% RH for $_{mono}$UiO-66. In comparison, the functionalization of the ligand with a hydrophilic functional group, such as $–NH_2$, leads to strong attraction between $–NH_2$ and water molecules since the $–NH_2$ group serves as an H-bond donor. We have explored before the impact of the host-guest and guest-guest interactions in the shape of the isotherms;[48] in this case, it involves the change in the isotherm's shape from Type V (i.e., S-shaped) to a combined Type I (i.e., from convex to concave) + Type IV, and the shift of the step found to 2%–16% RH for $_{mono}$UiO-66-NH_2.[20,49] In addition to the increased interaction, the addition of the $–NH_2$ functional group can also impart strain on the structure, giving way to linker

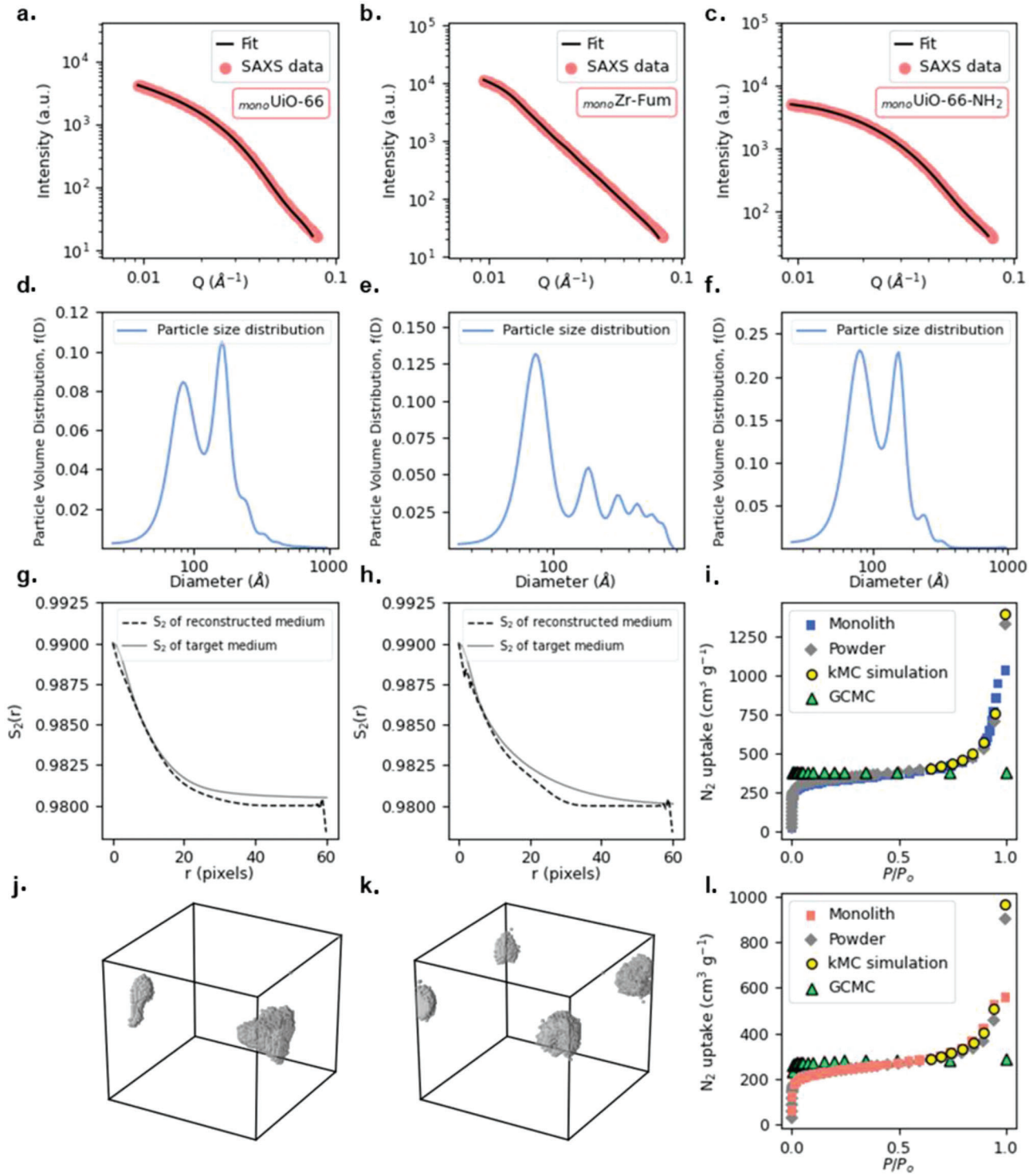

Figure 3. a–l) SAXS experimental data, SAXS fitting, and particle size distributions for $_{mono}$UiO-66, $_{mono}$Zr-fumarate, and $_{mono}$UiO-66-NH_2 (a–f) + Lattice-gas model reconstruction and molecular simulations for $_{mono}$Zr-fumarate and $_{mono}$UiO-66 (g–l). Experimental SAXS data is shown in red (circles) and fitting is shown in black (line) for $_{mono}$UiO-66 (a), $_{mono}$UiO-66-NH_2 (b), and $_{mono}$Zr-fumarate (c). Particle size distribution is shown in blue (line) for $_{mono}$UiO-66 (d), $_{mono}$UiO-66-NH_2 (e), and $_{mono}$Zr-fumarate (f). Comparison of S_2(r) functions of the target (gray line) and reconstructed medium (black dashed line) for $_{mono}$Zr-fumarate (g) and $_{mono}$UiO-66 (h). Reconstructed 3D realization of $_{mono}$UiO-66 (j) and $_{mono}$Zr-fumarate (k) defined on a bcc lattice with periodic boundaries; gray (white) voxels represent the solid (void) phase. The size of the system is 60 × 60 × 60 pixels for the 3D realization. Comparison of the experimental adsorption isotherms to simulated adsorption isotherms of N_2 at 77 K for UiO-66 (i) and Zr-fumarate (l); monolith—squares (blue for UiO-66 and orange for Zr-fumarate); powder—diamonds (gray); kMC simulations within the lattice-gas model—circles (yellow), and GCMC simulations—triangles (green).

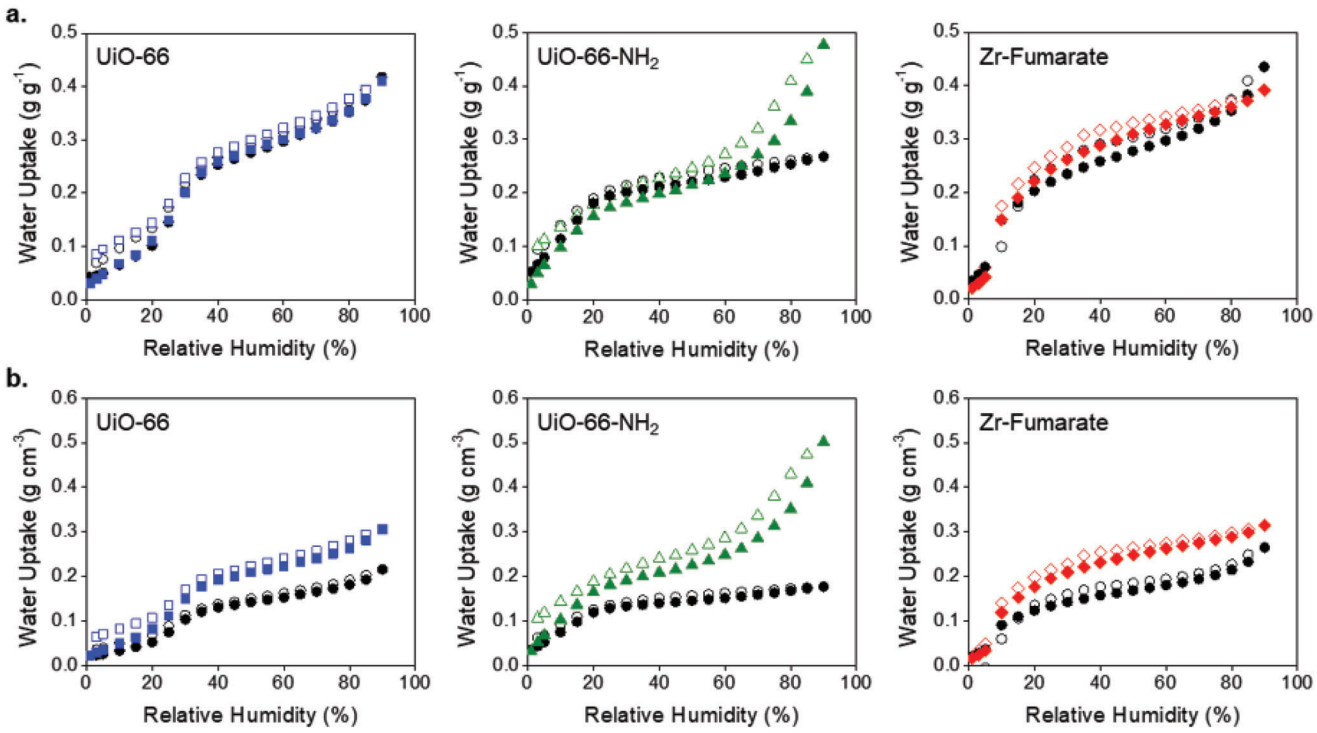

Figure 4. a,b) Comparison of gravimetric (a) and volumetric (b) water adsorption isotherms of $_{mono}$UiO-66 (blue squares), $_{mono}$UiO-66-NH_2 (green triangles), and $_{mono}$Zr-fumarate (red diamonds) at 25 °C. Water adsorption isotherms for corresponding powdered materials are represented by black circles. Adsorption and desorption isotherms are represented by closed and open markers, respectively.

rotation and an overall reduction of the pore size, hence increasing the hydrophilicity of the material.[28]

Table 1 compares the gravimetric and volumetric water uptake of the materials at 10%, 30%, and 90% RH at 25 °C. The gravimetric water adsorption isotherms of the powder and monolithic samples display similar shapes and uptakes. The exception is $_{mono}$UiO-66-NH_2, which exhibits extensive water uptake at higher relative humidity compared to $_{powd}$UiO-66-NH_2 (Figure 4a). This large water uptake can be attributed to the additional meso-/macroporosity in the monolithic variant observed in the N_2 adsorption isotherm (Figure S6a, Supporting Information). In contrast to the gravimetric data, the monoliths exhibit much higher volumetric adsorption performance compared to their powder counterparts thanks to their combined high ρ_b and S_{BET} (Figure 4b). $_{mono}$UiO-66, $_{mono}$UiO-66-NH_2, and $_{mono}$Zr-fumarate showed 50%, 46%, and 50%, higher volumetric water capacity at 30% RH than their powdered forms, respectively (Table 1).

We also looked at adsorption kinetics while collecting the water adsorption isotherms. Figure S20, Supporting Information, shows the adsorption and desorption kinetics of the powder and monolithic materials; we also converted this data to volumetric units for comparison. $_{powd}$UiO-66-NH_2 with its –NH_2 hydrophilic groups were faster than $_{mono}$UiO-66-NH_2 to complete one adsorption–desorption cycle (4000 min). Indeed, $_{mono}$UiO-66-NH_2 showed slower desorption kinetics than $_{powd}$UiO-66-NH_2 (6250 min). However, when comparing the amount adsorbed at a given time and calculating the gradients, $_{mono}$UiO-66-NH_2 reached saturation pressure at ca. 30% RH slightly faster (1.9×10^{-4} g g^{-1} min^{-1}) than $_{powd}$UiO-66-NH_2 (1.7×10^{-4} g g^{-1} min^{-1})—in other words, the monolithic material adsorbs more water per minute than the powder gravimetrically and volumetrically (**Figure 5**a,b). The kinetics of adsorption is highly dependent not only on the interaction between water and the internal surface with the specific ligands but also on the packing of the primary particles, and therefore the intrinsic and extrinsic porosity of the monoliths. Importantly, the impact of the ligand effect, and in this case the hydrophilic –NH_2 groups, is better observed in the monoliths than in the powdered MOFs. We hypothesize this is due to the denser packing of the MOF primary particles where the water molecules must travel through the intrinsic and extrinsic pore network during the adsorption and desorption processes. In contrast, in the case of the powder, water goes through the interstitial voids between the particles and is less exposed to the molecular design of the internal porosity.

In the case of UiO-66, saturation takes place at 40% RH. $_{mono}$UiO-66 showed slower adsorption kinetics (1.3×10^{-4} g g^{-1} min^{-1}) than the powder version (1.7×10^{-4} g g^{-1} min^{-1}), whereas desorption kinetics were similar. The slower kinetics might be caused by the densely packed hydrophobic nature of the ligand and pores. However, when looking at the adsorption gradients and the amount of water adsorbed per minute, $_{mono}$UiO-66 shows similar results (1.0×10^{-4} g cm^{-3} min^{-1}) to that of $_{powd}$UiO-66 (0.9×10^{-4} g cm^{-3} min^{-1}) due to the higher volumetric water uptake between 0 and 40% RH (Figure 5c,d). For, Zr-fumarate, although equilibration for $_{mono}$Zr-fumarate is slower (2.0×10^{-4} g g^{-1} min^{-1}) than for the powder (2.8×10^{-4} g g^{-1} min^{-1}) in the 0–30% RH region, both versions took the same time to complete

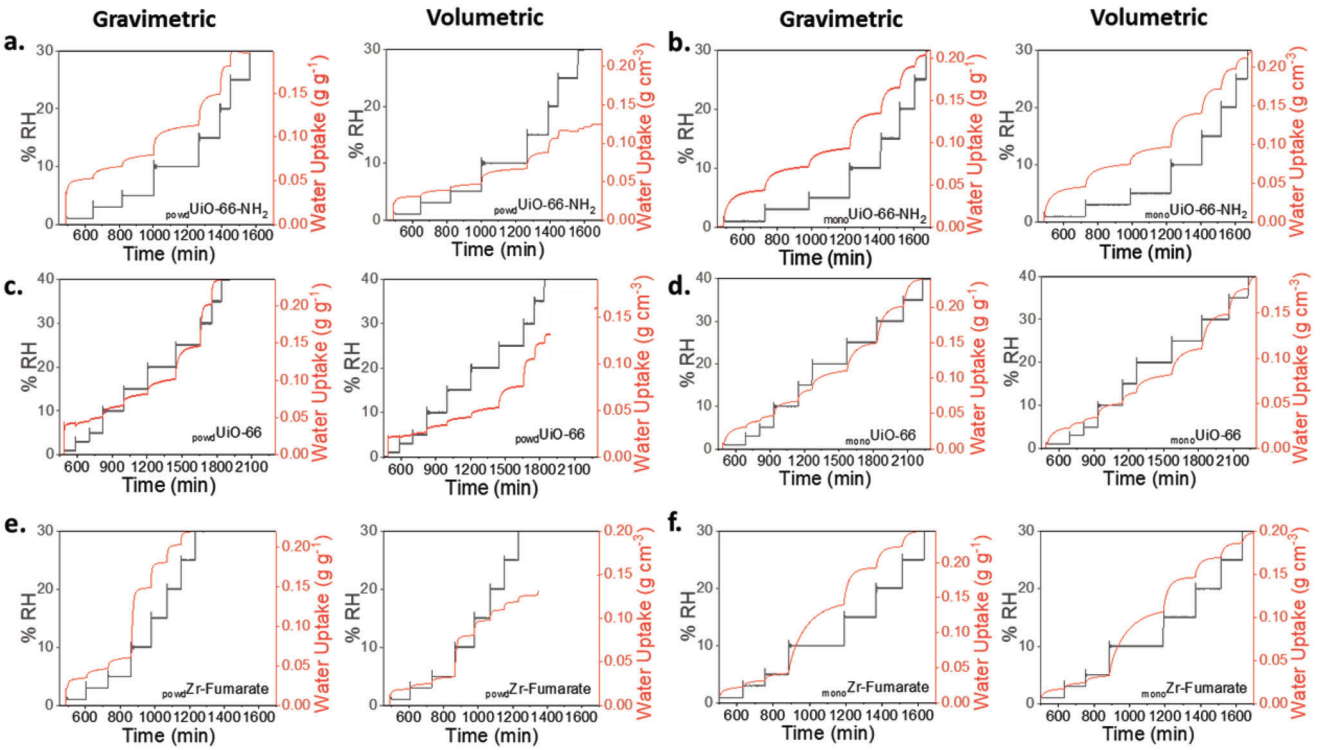

Figure 5. a–f) Gravimetric (first column) and volumetric (second column) water adsorption kinetics up to defined saturation pressure for powder($_{powd}$UiO-66-NH$_2$ (a), $_{powd}$UiO-66 (c), $_{powd}$Zr-fumarate (e)) and monolith ($_{mono}$UiO-66-NH$_2$ (b), $_{mono}$UiO-66 (d), $_{mono}$Zr-fumarate (f)) Zr-MOFs.

one adsorption and desorption cycle (4500 min). Again, when looking at the amount of water adsorbed per minute, volumetrically, $_{mono}$Zr-fumarate (1.7×10^{-4} g cm^{-3} min^{-1}) shower steeper gradients than $_{powd}$Zr-fumarate (1.5×10^{-4} g cm^{-3} min^{-1}) (Figure 5e,f). All in all, $_{mono}$Zr-fumarate (4500 min) was the fastest to finish one adsorption–desorption cycle compared to $_{mono}$UiO-66 (6250 min) and $_{mono}$UiO-66-NH$_2$ (6200 min) (Figure S20, Supporting Information).

The water adsorption properties of the $_{mono}$MOFs prompted us to further examine these materials for adsorption chiller applications at low regeneration temperatures (<100 °C). This is essential for the utilization of modest energy sources such as industrial waste heat and solar heat instead of electricity.[50] Initially, variable temperature water adsorption isotherms (25 and 40 °C) (Figure S21, Supporting Information) were collected to calculate the enthalpy of adsorption, ΔH_{ads}, using the Clausius–Clapeyron equation (Equation S16, Supporting Information). **Figure 6**a shows its evolution with the vapor uptake. First, $_{mono}$UiO-66 displays a high ΔH_{ads} in absolute terms at low coverage (−60 kJ mol^{-1}), dropping to −35 kJ mol^{-1} at an uptake value of ca. 10 wt.% before stabilizing at ca. −40 kJ mol^{-1} from 15 wt. % until saturation. In contrast, $_{mono}$UiO-66-NH$_2$ displays a high ΔH_{ads} in absolute terms of (−108 kJ mol^{-1}), confirming our previous observation on the shape of the isotherm. Again, the high ΔH_{ads} can be attributed to the presence of hydrophilic –NH$_2$ functional groups within the material.[20,47,48] Conversely, the ΔH_{ads} of $_{mono}$Zr-fumarate remained around −50 kJ mol^{-1}, showing a value closer to that of the enthalpy of evaporation of water, and making it an excellent candidate for this application.

We also used the variable-temperature isobars of each $_{mono}$MOF to calculate the COP for cooling. The COP for cooling is defined as the useful produced energy divided by the energy required, namely the ratio of vaporization heat (Q_{ev}) to regeneration heat (Q_{reg}) (Equations S11–S16, Supporting Information).[51] To evaluate both Q_{ev} and Q_{reg}, we calculated the heat capacity (c_p) of the monoliths as a function of the temperature of desorption (T_{des}) through a differential scanning calorimeter (Figure S22, Supporting Information). To determine the volumetric working capacities (Δw) of the working pairs $_{mono}$MOF/water pairs, we analyzed the isosteric cycle diagrams of the adsorption, air-conditioning cycle separately. Importantly, Δw is defined as the difference between the maximum (w_{max}) and minimum water uptakes (w_{min}). Figure 6b–d shows the cycle diagrams for the monolithic MOF/water pairs, shown by the points from I to IV, and calculated using the water adsorption isobars in a range of vapor pressure values (0.7, 1.2, 2.4, 3.7, and 5.6 kPa) and under variable T_{des} (Figure S23, Supporting Information) with the operational temperature of the cycle evaporation (T_{ev}) fixed at 10 °C, and the temperatures of adsorption (T_{ad}) and condensation (T_{con}) both fixed at 30 °C. In this cycle, the working capacity (Δw) depends on the T_{des}. Once we had determined the Δw, T_{des}, c_p, and ΔH_{ads} parameters, we calculated the COP as a function of T_{des}.

Figure 7a–c shows the volumetric Δw and COP as a function of T_{des}, with COP values of 0.66, 0.40, and 0.71 for $_{mono}$UiO-66, $_{mono}$UiO-66-NH$_2$, and $_{mono}$Zr-fumarate, respectively. The maximum working capacities at T_{des} of 100 °C were 0.08, 0.12, and 0.15 cm^3 cm^{-3}. Despite its hydrophilic nature, $_{mono}$UiO-66-NH$_2$ has the lowest COP value (0.40) and working capacity (0.12 at

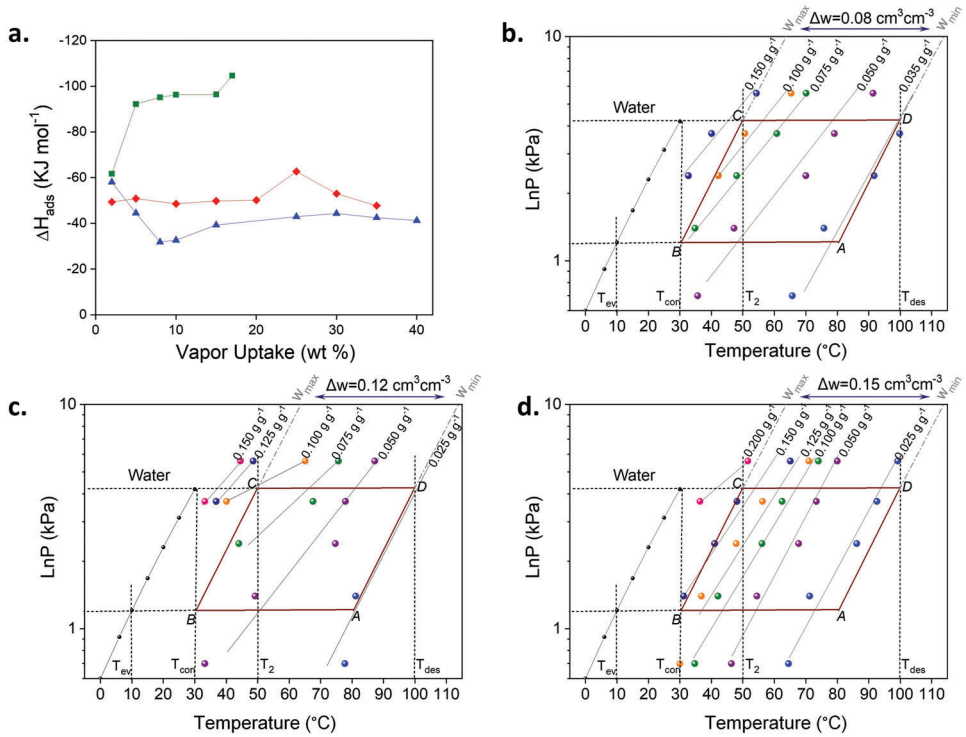

Figure 6. a) Enthalpy of adsorption as a function of loading for $_{mono}$UiO-66 (blue triangles), $_{mono}$UiO-66-NH_2 (green squares), and $_{mono}$Zr-fumarate (red diamonds). b–d) Isosteric cycle diagram for the working pairs $_{mono}$UiO-66/water (b), $_{mono}$UiO-66-NH_2/water (c), and $_{mono}$Zr-fumarate/water (d) calculated for an air-cooling cycle including the volumetric working capacity calculated considering the bulk density of the $_{mono}$MOFs. The colored dots on the isosteric diagrams represent the certain temperatures (from 30 to 100 °C see Figure S23, Supporting Information) for the indicated water uptake in a range of vapor pressure values (0.7, 1.2, 2.4, 3.7, and 5.6 kPa) found by using the isobars (Figure S23, Supporting Information) Points A–D show the flow of the process, where (B to C) is the isosteric heating, (C to D) is the isobaric desorption, (D to A) is the isosteric cooling, and (A to B) is the isobaric adsorption.

100 °C). This behavior in $_{mono}$UiO-66-NH_2 can be attributed to the high –NH_2···H_2O interactions as illustrated by the shape of the isotherm and the ΔH_{ads} calculations, resulting in high regeneration requirements (Figure 6a). The working capacity of $_{mono}$UiO-66 at low temperatures (0.03 and 0.05 cm^3 cm^{-3} for T_{des} of 60 and 70 °C, respectively) is slightly higher than that of $_{mono}$UiO-66-NH_2 (0.03 and 0.04 cm^3 cm^{-3} for T_{des} of 60 and 70 °C, respectively) but, overall, it suffers from its hydrophobic nature, showing the lowest working capacity of the three materials at 100 °C (0.08 cm^3 cm^{-3}) (Figure 7a). The $_{mono}$Zr-fumarate material shows the best performance with a working capacity of 0.15 cm^3 cm^{-3} at 100 °C (Figure 7c), with a remarkably high COP, equivalent to its powder form.[52]

To examine the stability of $_{mono}$Zr-fumarate for HVAC applications, we carried out cycling tests over 50 consecutive water adsorption–desorption cycles (Figure 7d and Figure S24, Supporting Information). The sample was cycled between 50 and 120 °C in a saturated water atmosphere to promote fast adsorption and desorption. The gravimetric uptake was found to decrease from 0.25 to 0.20 g g^{-1} (ca. 20%) over 45 cycles, reaching later a plateau. We extended it to 50 cycles (i.e., 5 additional ones) to make sure that the uptake is stable at 0.20 g g^{-1} (Figure 7e). The $_{mono}$Zr-fumarate was subsequently analyzed using PXRD and 77 K N_2 adsorption. The BET area decreased by 10% after the 50 cycles, whereas the PXRD confirmed the crystalline phase of Zr-fumarate (Figure 7f and Figure S25, Supporting Information).

Finally, we compared the performance of our $_{mono}$MOFs within the benchmark powder materials found in the literature such as Ni_2Cl_2BBTA and Co_2Cl_2BBTA,[53,54] Zr-fumarate [52], Al-fumarate,[55] MIP-200,[23] SAPO-34,[27] MIL-160,[56] and CAU-10.[57] Among these benchmarks, Al-fumarate and SAPO-34 have been reported in pelletized form with a density of 0.61[55] and 0.70[58] g cm^{-3}, respectively. The other materials have not been shaped and/or the bulk densities of the shaped bodies have not been reported in the literature. The powder materials cannot be used in AHT systems therefore shaping and densification are crucial. It has been reported that bulk density yields 50% lower than the theoretical crystal density after pelletization for several MOFs.[39,59,60] Therefore, we divided the crystal densities by half to estimate the pellet densities, enabling us to compare the volumetric capacity of the benchmark materials with that of our $_{mono}$MOFs and compacted MOF pellets. We estimated the pellet densities of the benchmark materials based on their crystal densities which are 1.16 g cm^{-3} for MIP-200, 1.10 g cm^{-3} for Ni_2Cl_2BTDD, 0.65 g cm^{-3} for Co_2Cl_2BTDD, 1.07 g cm^{-3} for MIL-160 and 1.15 g cm^{-3} for CAU-10. To do the comparison, first, we plot the gravimetric water sorption isotherm at 25 °C (**Figure 8**a) and then the volumetric water sorption isotherm at 25 °C (Figure 8b) based on the reported or the estimated pellet

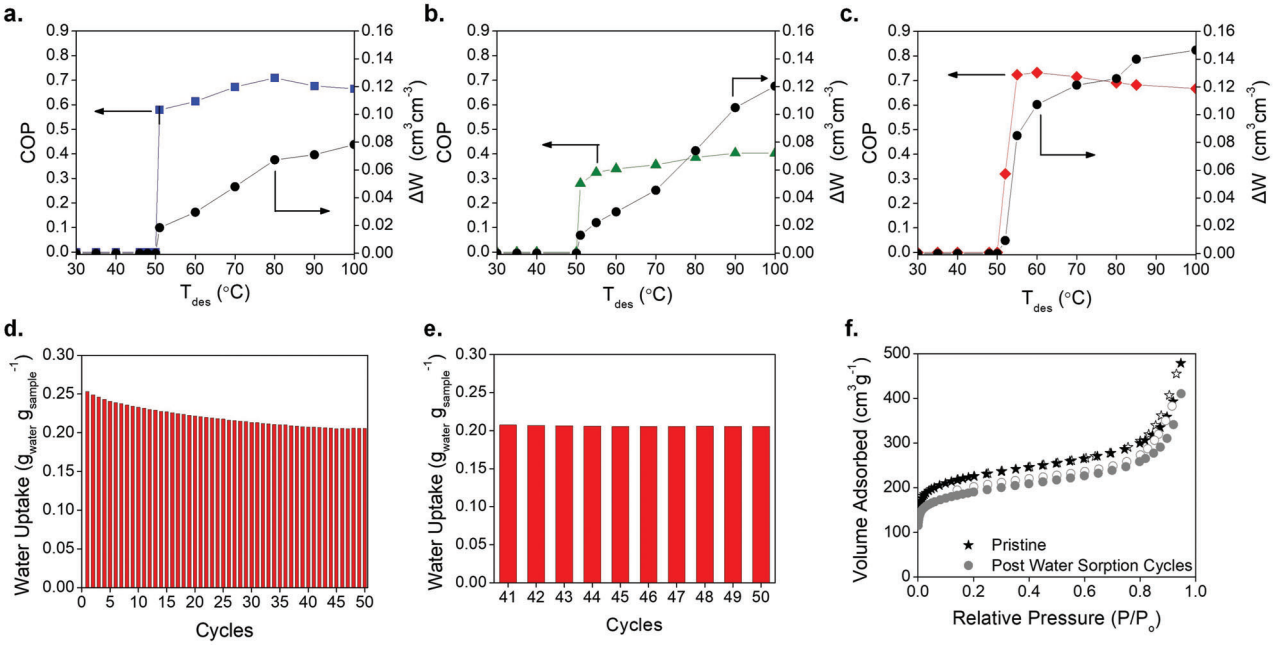

Figure 7. a–c) COP for cooling and volumetric working capacity (Δw) as a function of T_{des} for $_{mono}$UiO-66 (a), $_{mono}$UiO-66-NH$_2$ (b), and $_{mono}$Zr-fumarate (c). d) $_{mono}$Zr-fumarate adsorption/desorption cycle testing performed over 50 consecutive cycles with regeneration at 120 °C. e) $_{mono}$Zr-fumarate adsorption/desorption cycle plot zoomed in between cycles 41st–50th with regeneration at 120 °C. f) 77 K N_2 adsorption/desorption isotherms for pristine (black stars) and post-water adsorption (gray circles) $_{mono}$Zr-fumarate.

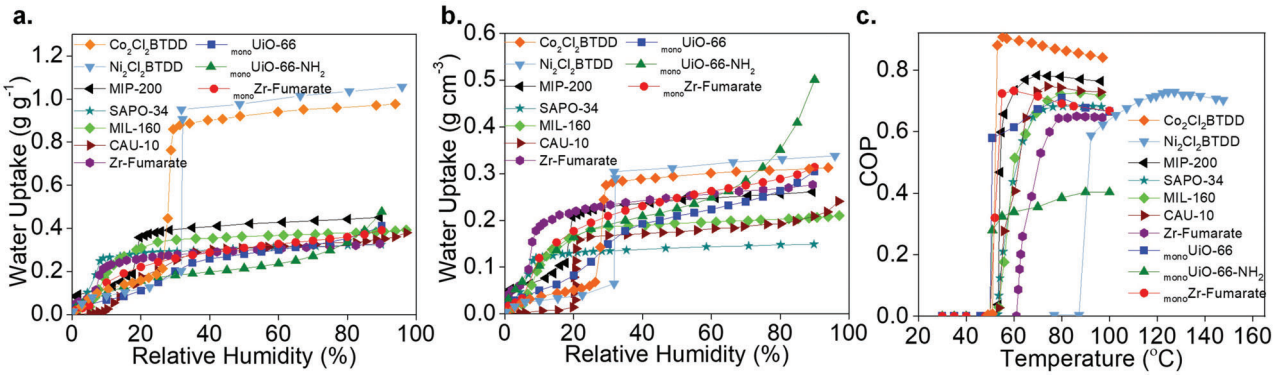

Figure 8. a) Gravimetric and b) estimated volumetric water adsorption performance comparison of $_{mono}$Zr-MOFs with powder benchmark adsorbents, measured at 25 °C. c) Corresponding COP values for chiller applications of $_{mono}$Zr-MOFs compared with powdered benchmark materials as a function of T_{des} (T_{ev} = 10 °C and T_{con} = 30 °C).

densities belonging to benchmark powder materials and the bulk density of our $_{mono}$MOFs. Our monolithic materials have excellent volumetric sorption capacities, even when compared to the estimated volumetric capacity of the benchmark pellet materials, which may be lower than their estimated bulk density. Especially, $_{mono}$Zr-fumarate displayed comparable COP for cooling to benchmark adsorbents for AHT systems (Figure 8c), being an excellent candidate with its green synthesis method to be commercialized for HVAC applications.

5. Conclusion

We have previously reported how $_{mono}$MOFs can form high-density shaped bodies whilst retaining their adsorption performance. The high bulk densities of $_{mono}$MOFs provide greater volumetric adsorption capacities when compared to their powdered and pelletized counterparts. Here, we have synthesized monoZr-MOFs, introducing an improved version of existing materials in terms of their shaped performance. Our monoliths can be synthesized on a multigram scale, preserving the adsorption capabilities after shaping. Moreover, we have visualized the monolithic structures across the mesoporous range using SAXS and lattice-gas models, giving accurate future predictions of the adsorption characteristics of the monolithic materials. This has allowed us to examine their performance for HVAC applications, comparing them to their experimental performance.

Among $_{mono}$Zr-MOFs studied, $_{mono}$Zr-fumarate stood out in overcoming the traditional limitations of MOF shaping

techniques. This method demonstrates that producing densely packed bodies is possible even for fragile MOFs that cannot be shaped by applied pressure without a significant decrease[34] in performance due to the pore collapse. $_{mono}$Zr-fumarate also showed excellent performance with exceptional volumetric performance and high COP for cooling (0.71 at 100 °C), being comparable with the reported benchmark materials as shown above (Figure 8).

High gravimetric uptake is crucial to be used in real-life applications as much as high volumetric capacity. Not only for, for example, vehicular applications (such as an HVAC system in a car) where the space is limited but also for any other system where the capex and opex can be minimized with smaller and more compact systems. Thus, the volumetric capacity of the MOF is critical. On top of that, even though MIP-200 and Co_2Cl_2BTDD seem to have higher COP values due to their high gravimetric uptake, they are still synthesized only as powders, which cannot be used in industrial applications at this stage. Also, when selecting optimal materials, the synthesis process of the selected material needs to be considered. The chemicals used in the synthesis procedure have an important effect on industrialization in terms of cost, efficiency, and toxicity of the process. Therefore, $_{mono}$Zr-fumarate demonstrates that $_{mono}$MOFs hold great promise for applications in next-generation, energy-efficient, adsorption-driven HVAC technologies.

Supporting Information

Supporting Information is available from the Wiley Online Library or from the author.

Acknowledgements

This project has received funding from the European Research Council (ERC) under the European Union's Horizon 2020 Research and Innovation Programme (NanoMOFdeli), ERC-2016-COG 726380, Innovate UK (104384) and EPSRC (EP/S009000/1). N.R. acknowledges support from the Cambridge International Scholarship and the Trinity Henry-Barlow Scholarship (honorary). D.F.-J. thanks the Royal Society for funding through a University Research Fellowship. The XPS facility and the Tecnai F20 TEM are supported through the Cambridge Royce facilities grant EP/P024947/1 and Sir Henry Royce Institute—recurrent grant EP/R00661X/1. J.S.A. would like to acknowledge financial support from Ministerio de Ciencia e Innovación (Project PID2019-108453GB-C21).

Note: The formatting of the header row of Table 1 was corrected on June 8, 2023, after initial publication online.

Conflict of Interest

C.Ç., R.B., and D.F.-J. have financial interests in the start-up company Immaterial, which is seeking to commercialize MOFs.

Data Availability Statement

The data that support the findings of this study are available from the corresponding author upon reasonable request.

Keywords

coefficient of performance, heating, ventilation, and air conditioning, metal–organic frameworks, renewable cooling, water adsorption

Received: October 3, 2022
Revised: March 7, 2023
Published online: April 21, 2023

[1] B. Dean, J. Dulac, T. Morgan, U. Remme, B. Motherway, The Future of Cooling: Opportunities for Energy-Efficient Air Conditioning International Energy Agency, **2018**, https://iea.blob.core.windows.net/assets/0bb45525-277f-4c9c-8d0c-9c0cb5e7d525/The_Future_of_Cooling.pdf.
[2] Y. Li, X. Wang, P. Luo, Q. Pan, *Energies* **2019**, *12*, 1494.
[3] J. Ni, X. Bai, *Renewable Sustainable Energy Rev.* **2017**, *67*, 625.
[4] B. J. van Ruijven, E. De Cian, *Nat. Commun.* **2019**, *10*, 2762.
[5] S. Cui, M. Qin, A. Marandi, V. Steggles, S. Wang, X. Feng, F. Nouar, C. Serre, *Sci. Rep.* **2018**, *8*, 15284.
[6] E. Hastürk, S. -J. Ernst, C. Janiak, *Curr. Opin. Chem. Eng.* **2019**, *24*, 26.
[7] X. Liu, X. Wang, F. Kapteijn, *Chem. Rev.* **2020**, *120*, 8303.
[8] J. Pérez-Carvajal, G. Boix, I. Imaz, D. Maspoch, *Adv. Energy Mater.* **2019**, *9*, 1901535.
[9] C. A. Balaras, G. Grossman, H.-M. Henning, C. A. Infante Ferreira, E. Podesser, L. Wang, E. Wiemken, *Renewable Sustainable Energy Rev.* **2007**, *11*, 299.
[10] H. - M. Henning, *Appl. Therm. Eng.* **2007**, *27*, 1734.
[11] M. B. Elsheniti, O. A. Elsamni, R. K. Al-dadah, S. Mahmoud, E. Elsayed, K. Saleh, in *Sustainable Air Conditioning Systems* (Eds.: C. Ghenai, T. Salameh), IntechOpen, London, UK **2018**, Ch. 4.
[12] A. Kumar, D. G. Madden, M. Lusi, K. - J. Chen, E. A. Daniels, T. Curtin, J. J. Perry IV, M. J. Zaworotko, *Angew. Chem., Int. Ed.* **2015**, *54*, 14372.
[13] M. Eddaoudi, J. Kim, N. Rosi, D. Vodak, J. Wachter, M. O'Keeffe, O. M. Yaghi, *Science* **2002**, *295*, 469.
[14] S. Kaskel, *Angew. Chem., Int. Ed.* **2010**, *49*, 9565.
[15] P. Z. Moghadam, A. Li, S. B. Wiggin, A. Tao, A. G. P. Maloney, P. A. Wood, S. C. Ward, D. Fairen-Jimenez, *Chem. Mater.* **2017**, *29*, 2618.
[16] P. Z. Moghadam, A. Li, X. - W. Liu, R. Bueno-Perez, S. - D. Wang, S. B. Wiggin, P. A. Wood, D. Fairen-Jimenez, *Chem. Sci.* **2020**, *11*, 8373.
[17] N. C. Burtch, H. Jasuja, K. S. Walton, *Chem. Rev.* **2014**, *114*, 10575.
[18] S. M. Towsif Abtab, D. Alezi, P. M. Bhatt, A. Shkurenko, Y. Belmabkhout, H. Aggarwal, Ł. J. Weseliński, N. Alsadun, U. Samin, M. N. Hedhili, M. Eddaoudi, *Chem* **2018**, *4*, 94.
[19] D. Fröhlich, S. K. Henninger, C. Janiak, *Dalton Trans.* **2014**, *43*, 15300.
[20] F. Jeremias, V. Lozan, S. K. Henninger, C. Janiak, *Dalton Trans.* **2013**, *42*, 15967.
[21] N. S. Hanikel, M. Prévot, F. A. Fathieh, E. Kapustin, H. Lyu, H. J. Wang, N. Diercks, T. M. Grant Glover, O. Yaghi, *ACS Cent. Sci.* **2019**, *5*, 1699.
[22] S. Chaemchuen, X. Xiao, N. Klomkliang, Yusubov, M. S. F. Verpoort, *Nanomaterials* **2018**, *8*, 661.
[23] S. Wang, J. S. Lee, M. Wahiduzzaman, J. Park, M. Muschi, C. Martineau-Corcos, A. Tissot, K. H. Cho, J. Marrot, W. Shepard, G. Maurin, J. - S. Chang, C. Serre, *Nat. Energy* **2018**, *3*, 985.
[24] M. H. Bagheri, S. N. Schiffres, *Langmuir* **2018**, *34*, 1908.
[25] B. Han, A. Chakraborty, *Energy Convers. Manage.* **2020**, *213*, 112825.
[26] S. Gökpinar, S. - J. Ernst, E. Hastürk, M. Möllers, I. el Aita, R. Wiedey, N. Tannert, S. Nießing, S. Abdpour, A. Schmitz, J. Quodbach, G. K. Füldner, S. Henninger, C. Janiak, *Ind. Eng. Chem. Res.* **2019**, *58*, 21493.
[27] A. Freni, L. Bonaccorsi, L. Calabrese, A. Caprì, A. Frazzica, A. Sapienza, *Appl. Therm. Eng.* **2015**, *82*, 1.
[28] M. J. Kalmutzki, C. S. Diercks, O. M. Yaghi, *Adv. Mater.* **2018**, *30*, 1704304.
[29] Y. I. Aristov, I. S. Glaznev, I. S. Girnik, *Energy* **2012**, *46*, 484.
[30] X. - M. Liu, L. - H. Xie, Y. Wu, *Inorg. Chem. Front.* **2020**, *7*, 2840.
[31] M. Rubio-Martinez, C. Avci-Camur, A. W. Thornton, I. Imaz, D. Maspoch, M. R. Hill, *Chem. Soc. Rev.* **2017**, *46*, 3453.

[32] T. Tian, Z. Zeng, D. Vulpe, M. E. Casco, G. Divitini, P. A. Midgley, J. Silvestre-Albero, J. - C. Tan, P. Z. Moghadam, D. Fairen-Jimenez, *Nat. Mater.* **2017**, *17*, 174.
[33] B. M. Connolly, D. G. Madden, A. E. H. Wheatley, D. Fairen-Jimenez, *J. Am. Chem. Soc.* **2020**, *142*, 8541.
[34] M. Taddei, M. J. McPherson, A. Gougsa, J. Lam, J. Sewell, E. Andreoli, *Inorganics* **2019**, *7*, 110.
[35] J. Dhainaut, C. Avci-Camur, J. Troyano, A. Legrand, J. Canivet, I. Imaz, D. Maspoch, H. Reinsch, D. Farrusseng, *CrystEngComm* **2017**, *19*, 4211.
[36] P. Z. Moghadam, S. M. J. Rogge, A. Li, C. - M. Chow, J. Wieme, N. Moharrami, M. Aragones-Anglada, G. Conduit, D. A. Gomez-Gualdron, V. Van Speybroeck, D. Fairen-Jimenez, *Matter* **2019**, *1*, 219.
[37] B. M. Connolly, M. Aragones-Anglada, J. Gandara-Loe, N. A. Danaf, D. C. Lamb, J. P. Mehta, D. Vulpe, S. Wuttke, J. Silvestre-Albero, P. Z. Moghadam, A. E. H. Wheatley, D. Fairen-Jimenez, *Nat. Commun.* **2019**, *10*, 2345.
[38] T. Tian, J. Velazquez-Garcia, T. D. Bennett, D. Fairen-Jimenez, *J. Mater. Chem. A* **2015**, *3*, 2999.
[39] D. G. Madden, D. O'Nolan, N. Rampal, R. Babu, C. Çamur, A. N. al Shakhs, S. Y. Zhang, G. A. Rance, J. Perez, N. Maria Casati, pietro, C. Cuadrado-Collados, D. O'Sullivan, N. P. Rice, T. Gennett, P. Parilla, S. Shulda, K. E. Hurst, V. Stavila, M. D. Allendorf, J. Silvestre-Albero, A. C. Forse, N. R. Champness, K. W. Chapman, D. Fairen-Jimenez, *J. Am. Chem. Soc.* **2022**, *144*, 13729.
[40] H. Furukawa, F. Gándara, Y. - B. Zhang, J. Jiang, W. L. Queen, M. R. Hudson, O. M. Yaghi, *J. Am. Chem. Soc.* **2014**, 4369.
[41] C. Avci-Camur, J. Perez-Carvajal, I. Imaz, D. Maspoch, *ACS Sustainable Chem. Eng.* **2018**, *6*, 14554.
[42] J. Osterrieth, J. Rampersad, D. G. Madden, N. Rampal, L. Skoric, B. Connolly, M. Allendorf, V. Stavila, J. Snider, R. Ameloot, J. Marreiros, C. Ania, D. Azevedo, E. Vilarrasa-García, B. F. Santos, X.-H. Bu, Z. Chang, H. Bunzen, N. R. Champness, S. L. Griffin, B. Chen, R.-B. Lin, B. Coasne, S. Cohen, J. C. Moreton, Y. J. Colón, L. Chen, R. Clowes, F.-X. Coudert, Y. Cui, et al., *Adv. Mater.* **2022**, *34*, 2201502.
[43] D. A. Gómez-Gualdrón, P. Z. Moghadam, J. T. Hupp, O. K. Farha, R. Q. Snurr, *J. Am. Chem. Soc.* **2015**, *138*, 215.
[44] G. C. Shearer, S. Chavan, S. Bordiga, S. Svelle, U. Olsbye, K. P. Lillerud, *Chem. Mater.* **2016**, *28*, 3749.
[45] M. J. Katz, Z. J. Brown, Y. J. Colón, P. W. Siu, K. A. Scheidt, R. Q. Snurr, J. T. Hupp, O. K. Farha, *Chem. Commun.* **2013**, *49*, 9449.
[46] L. Gelb, K. Gubbins, R. Radhakrishnan, M. Sliwinska-Bartkowiak, *Rep. Prog. Phys.* **1999**, *62*, 1573.
[47] R. Evans, *J. Phys.: Condens. Matter* **1990**, *2*, 8989.
[48] D. A. Fairen-Jimenez, N. Seaton, T. Düren, *Langmuir* **2010**, *26*, 14694.
[49] J. Canivet, J. Bonnefoy, C. Daniel, A. Legrand, B. Coasne, D. Farrusseng, *New J. Chem.* **2014**, *38*, 3102.
[50] M. Chorowski, P. Pyrka, *Energy* **2015**, *92*, 221.
[51] M. F. de Lange, K. J. F. M. Verouden, T. J. H. Vlugt, J. Gascon, F. Kapteijn, *Chem. Rev.* **2015**, *115*, 12205.
[52] M. V. Solovyeva, L. G. Gordeeva, T. A. Krieger, Y. I. Aristov, *Energy Convers. Manage.* **2018**, *174*, 356.
[53] A. J. Rieth, A. M. Wright, S. Rao, H. Kim, A. D. LaPotin, E. N. Wang, M. Dincă, *J. Am. Chem. Soc.* **2018**, *140*, 17591.
[54] A. J. Rieth, A. M. Wright, M. Dincă, *Nat. Rev. Mater.* **2019**, *4*, 708.
[55] F. Jeremias, D. Fröhlich, C. Janiak, S. K. Henninger, *RSC Adv.* **2014**, *4*, 24073.
[56] A. Cadiau, J. S. Lee, D. Damasceno Borges, P. Fabry, T. Devic, M. T. Wharmby, C. Martineau, D. Foucher, F. Taulelle, C. H. Jun, Y. K. Hwang, N. Stock, M. F. De Lange, F. Kapteijn, J. Gascon, G. Maurin, J. S. Chang, C. Serre, *Adv. Mater.* **2015**, *27*, 4775.
[57] M. F. de Lange, T. Zeng, T. J. H. Vlugt, J. Gascon, F. Kapteijn, *CrystEngComm* **2015**, *17*, 5911.
[58] M. Kim, H. - J. Chae, T. - W. Kim, K. - E. Jeong, C. - U. Kim, S. - Y. Jeong, *J. Ind. Eng. Chem.* **2011**, *17*, 621.
[59] Y. Peng, V. Krungleviciute, I. Eryazici, J. T. Hupp, O. K. Farha, T. Yildirim, *J. Am. Chem. Soc.* **2013**, *135*, 11887.
[60] J. Purewal, M. Veenstra, D. Tamburello, A. Ahmed, A. J. Matzger, A. G. Wong-Foy, S. Seth, Y. Liu, D. J. Siegel, *Int. J. Hydrogen Energy* **2019**, *44*, 15135.